

Innovative Methodology for the Synthesis of CoFe_2O_4 Encapsulated $\text{La}_2\text{Fe}_2\text{O}_6$ Nanoparticles for their Use in Various Applications.

Ebtesam. E. Ateia

Cairo University

Amira. T. Mohamed (✉ atawfik@sci.cu.edu.eg)

Cairo University <https://orcid.org/0000-0001-5351-5540>

Research Article

Keywords: Double perovskite, Spinel, Core shell, exchange coupling, metal removal capacity

Posted Date: November 30th, 2021

DOI: <https://doi.org/10.21203/rs.3.rs-1112104/v1>

License: © ⓘ This work is licensed under a Creative Commons Attribution 4.0 International License.

[Read Full License](#)

Abstract

It would be helpful to achieve appropriate synthetic routes to attain larger-scale production at industrial levels of nanocomposites at low costs. In the present work, diphasic composites with core-shell nanostructures formed by $\text{La}_2\text{Fe}_2\text{O}_6/\text{CoFe}_2\text{O}_4$ are investigated. The core-shell structure is fabricated via different preparation methods. The advantages and the demerits of the synthesis techniques are discussed. The presence of both the spinel CoFe_2O_4 nano ferrite and orthorhombic $\text{La}_2\text{Fe}_2\text{O}_6$ perovskite phases is revealed by X-ray diffraction (XRD). XPS spectroscopy is utilized to investigate the chemical composition of the prepared samples. The hysteresis loops of the prepared samples exhibit a smooth loop that is resulted from the existence of two homogeneous magnetic phases. For the first time, it has been found that the preparation conditions have the advantage of reducing the switching field distribution (SFD) value for the core-shell nanoparticles. Exchange coupled core-shell nanoparticles present a high potential to regulate the magnetic properties for numerous applications such as heavy metal removal and/or data storage devices. The maximum adsorption capacity (q_m) of Cr III on the core-shell (S3) is higher compared to other adsorbents previously testified in the literature. The cost-effective and eco-friendly prepared core-shell samples with good metal removal capacity have great potential for commercialization.

1. Introduction

Nowadays, the coating of nano ferrite particles on materials with various structures is a novel and motivating technique to synthesize multifunctional materials. New functionalities can be added to the core owing to the coated shell properties [1]. The core/shell formulism has a remarkable potential for use in biomedicine and energy storage devices [2–4]. In general, Core/shell particles are made up of an interior material (core) and an outer layer material (shell) [5].

Both core and shell could be fabricated from various categories of inorganic or organic materials as inorganic-inorganic, inorganic-organic, organic-inorganic as well as organic-organic [6–8].

Materials are crystallized in various crystal classes and structural families. The perovskite structure (ABO_3) is the host of a large number of transition metal oxides with novel physical properties [9, 10]. Furthermore, the double perovskite structure ($\text{A}_2\text{BB}'\text{O}_6$) can be formed through the alignment of respective bonding in the ABO_3 structure. The soft ferromagnetic nature, multiferroicity, and colossal magnetoresistance are occurred due to B B' super-exchange interactions and the ordering between B and B' [11–13]. As a result, the double perovskite structure is worth paying attention owing to its promising technological applications.

In the family of spinel structures, CoFe_2O_4 is of extreme prominence substance which exhibits remarkable properties like high magnetization, high coercivity, and high magneto crystalline anisotropy [14–16]. The hard nature of CoFe_2O_4 distinguishes it from other members.

Generally, the preservation of core–shell structures for the studied samples is the main issue. The perfect core–shell structure does not fundamentally lead to core–shell nano composites. This can be attributed to many parameters as lattice mismatch, dissimilar sinterability, aggregation, and interfacial diffusion. Additionally, numerous issues, besides the shape of the sample, are defining the required features of the attained product.

In this regard, CoFe_2O_4 seems to be appropriate in manufacturing composites using $\text{La}_2\text{Fe}_2\text{O}_6$ in a core – shell formulism. Up to now, core–shell nanoparticles using magnetic materials as the core and/or shell have been testified in order to tune the magnetization of the product [17–22].

To the best of our knowledge, no prior studies have been conducted on double perovskite spinel core shell. The aim of the present work is to synthesize $\text{La}_2\text{Fe}_2\text{O}_6/\text{CoFe}_2\text{O}_4$ core/shell nanoparticles with various preparation approaches. The core/shell multifunctional nanocomposites specifically with unique physiochemical properties are investigated.

The specific objective is to investigate the effectiveness of studied nanoparticles for Cr III adsorption from wastewater using i) Adsorption isotherms, and ii) Adsorption kinetics studies.

2. Experimental Work

2.1 Preparation of $\text{La}_2\text{Fe}_2\text{O}_6$ and CoFe_2O_4 nanoparticles

$\text{La}(\text{NO}_3)_3 \cdot 6\text{H}_2\text{O}$, $\text{Fe}(\text{NO}_3)_3 \cdot 9\text{H}_2\text{O}$, $\text{Co}(\text{NO}_3)_2 \cdot 6\text{H}_2\text{O}$, and citric acid with high purity (99.999%) were employed as starting reagents. All of the chemicals employed in the synthesis were assessed analytically. A modified citrate auto combustion technique was used to prepare $\text{La}_2\text{Fe}_2\text{O}_6$ and CoFe_2O_4 samples. The technical information about sample preparation procedures was previously mentioned [23, 24].

2.2 Preparation of $\text{La}_2\text{Fe}_2\text{O}_6/\text{CoFe}_2\text{O}_4$ core–shell structure

The individual preparation of core and shell layers separately are the main stages to prepare the core-shell nanoparticles. Three classes were used to prepare a core-shell nanoparticle according to different issues as illustrated in Fig. 1: a-c. S1 composite powder was attained via the addition of Fe^{3+} , Co^{2+} , and citric acid aqueous solution to the prepared $\text{La}_2\text{Fe}_2\text{O}_6$ in order to achieve nano composites.

During the synthesis of CoFe_2O_4 nanoparticles at constant pH, the $\text{La}_2\text{Fe}_2\text{O}_6$ was added to the gel of CoFe_2O_4 . The formation of the core-shell $\text{CoFe}_2\text{O}_4/\text{La}_2\text{Fe}_2\text{O}_6$ (S2) was obtained.

In Fig. 1:c the $\text{La}_2\text{Fe}_2\text{O}_6$ and CoFe_2O_4 (S3) precursors are adequately mixed to acquire superfine coated nanoparticles. Several tools were used to attain the target of mixing including solution dispersion, stirring, and grinding.

2.3 Sample analysis and characterizations

X-ray powder diffraction pattern (XRD) with a diffractometer (X'Pert PRO PANalytical, Netherland) was used to collect X-ray diffraction patterns of the synthesized samples. High-Resolution Transmission Electron Microscopy (HRTEM) was utilized to study the morphology and nanostructure of the materials utilizing the Tecnai G20, Super twin, double tilt model. Energy dispersive X-ray Analyses (EDAX) were carried out using SEM Model Quanta 250 FEG attached with EDAX unit.

X-ray photoelectron spectroscopy (XPS) was used to examine the chemical states of numerous elements in the prepared samples via monochromatic X-ray Al K-alpha radiation. A vibrating sample magnetometer (VSM) Model Lake Shore 7410 was utilized to measure the magnetization (emu/g) at room temperature (300 K).

3. Results And Discussion

Figure 2 displays the XRD pattern of the prepared core-shell samples. The observed peaks at 2θ values of 23.8° , 32.58° , 40.05° , 46.54° , 52.38° , 57.84° , and 67.57° are matched with ICDD no. 01-074-2203. These peaks correspond to the orthorhombic (Pbnm) distorted perovskite structure of $\text{La}_2\text{Fe}_2\text{O}_6$. While small new peaks emerged indicates the presence of another phase. Vertical dotted lines in the figure indicate the positions of these peaks. It is found that the peaks 30.25° , 35.5° , 43.38° , and 62.99° correspond to CoFe_2O_4 with space group Fd3m and matched with ICDD no. 04-005-7078. XRD pattern of the $\text{CoFe}_2\text{O}_4/\text{La}_2\text{Fe}_2\text{O}_6$ nanoparticles displays only the diffraction peaks of the perovskite phase for S1 in spite of EDAX confirms the presence of all expected elements. The obtained data for the samples designates that, there are mixing phases between the ingredients of the nanocomposite powders. This means a strong interdiffusion can occur between the CoFe_2O_4 and $\text{La}_2\text{Fe}_2\text{O}_6$ phases.

Additionally, the peaks belonging to the shell of CoFe_2O_4 as well as the core of $\text{La}_2\text{Fe}_2\text{O}_6$ are detected for S3. The functionalization of CoFe_2O_4 and $\text{La}_2\text{Fe}_2\text{O}_6$ encourages the creation of a core-shell structure. While the incomplete coating of the core CoFe_2O_4 is the main issue of the second sample S2 as ratified from HRTEM images.

No impurity phases are detected. The pattern reveals the presence of both the cubic spinel ferrite CoFe_2O_4 and orthorhombic $\text{La}_2\text{Fe}_2\text{O}_6$ perovskite phases which confirm the formation of the core-shell nanoparticles.

The HRTEM images are achieved for the studied samples as illustrated in Fig. (3: a-m). The particle size histograms of nanocomposites are depicted in Fig. 3: c, f, m. A Gaussian distribution is used to fit the histogram of the samples.

The samples prepared by numerous techniques have vital differences in the shape, size, and agglomeration although they have the same composition. This difference is elucidated on the basis of the phenomenological thermodynamic model [25]. This model is based on the interface energy between

the samples. Changing the preparation method will change the surface energy as well as the deposition proceeds in various ways.

The S1 sample has two phases as detected in HRTEM images (Fig. 3: d, e). The base phase is the highly agglomerates CoFe_2O_4 with numerous sizes attached to the $\text{La}_2\text{Fe}_2\text{O}_6$ nanoparticles

It is easily seen that the S2 nanoparticle samples consist of two different shapes; the first one is $\text{La}_2\text{Fe}_2\text{O}_6$ with an orthorhombic structure. While the second is CoFe_2O_4 with a cubic spinel structure. The incomplete coating of the core CoFe_2O_4 is an issue of the second technique which is a disadvantage of this technique. The morphology of the samples as shown in Fig. 3:(g, h) prove that the core material is not covered completely by $\text{La}_2\text{Fe}_2\text{O}_6$ nanocomposites. High porosity and low homogeneity with a high amount of pores are detected for S2 sample as shown in Fig. 3: h. Additionally, quite non-uniform morphology and highly agglomeration of the core nanoparticles can also be seen for sample S2. Vander Waals forces between the nanoparticles are the main reason for the observed agglomeration. This means that high energy is needed to separate the agglomerated particles [26]. While the S3 is formed of CoFe_2O_4 as a shell that completely covered the core of $\text{La}_2\text{Fe}_2\text{O}_6$.

The configuration and stoichiometry of the Core/Shell compounds are investigated using EDAX analysis (Fig. 4: a-c). The presence of intense O, La, and Fe peaks as well as a distinct Co peak ratifies the successful preparation of the $\text{La}_2\text{Fe}_2\text{O}_6/\text{CoFe}_2\text{O}_4$ Core/Shell / or nanocomposites. Additionally, the presence of a strong Co peak for the S3 sample ratify the formation of complete core-shell compared with the other two samples.

It also clear that no impurities are observed which strongly ratify the high crystalline nature of all the examined samples and this is also obvious from the XRD illustrated in Fig. 2.

To scrutinize the chemical composition of the investigated samples, XPS spectroscopy is studied. Fig. 5: a illustrates the survey spectrum of $\text{La}_2\text{Fe}_2\text{O}_6/\text{CoFe}_2\text{O}_4$ core-shell which ratify the existence of La, Fe, Co, and O elements in the prepared composites. The spectra of Fe 2p are split into two spin-orbit doublets, which correspond to Fe 2p_{3/2} and Fe 2p_{1/2}, respectively (Fig. 5: b). The low energy Fe 2p_{3/2} peak is fitted with two peaks, both of which are associated with Fe^{3+} ions at the Oh and Td sites [27]. Though, the peak positions for Fe 2p_{3/2} and Fe 2p_{1/2} sub-spectra corresponding to Fe^{3+} in B-sites and its satellites match with that expected for Fe^{2+} . Consequently, the B positions can be occupied either by Fe^{2+} or Fe^{3+} cations. Besides, the presence of Fe^{2+} is identified by feature peaks that are detected for S1, S2, and S3 at 716.57, 716.23 and 716.53 respectively are corresponding to the presence of Fe^{2+} cation [28–30]. The high-resolution Co 2p spectrum, depicted in Fig. 5:c, consists of two spin-orbit doublets Co 2p_{3/2} characterized for Co^{2+} , and Co^{3+} in B-sites [31, 32]. While the detected Co 2p_{1/2} peak is categorized for Co^{2+} in B sites.

Finally, the existence of Co and Fe ions in the +3, +2 oxidation states reveal the phase stabilization of the prepared $\text{La}_2\text{Fe}_2\text{O}_6/\text{CoFe}_2\text{O}_4$ double-perovskite composites.

The O 1s spectrum is split into multi peaks for all studied samples as shown in Fig. 5: d. The low binding energy B.E. < 530 eV is due to the Fe/Co–O bond [31]. The peaks with high B.E. >530 eV can be due to surface oxygen species of lattice defects [31, 32]. According to ZHAO Kun et.al [33], those peaks are attributed to the adsorbed oxygen (O_2^{2-} , O_2^{1-}) which is interrelated to the oxygen vacancies.

The various nano composites are examined by using the *M-H* hysteresis loop as illustrated in Fig. 6:(a-c). The magnetization of the samples is greatly influenced by the interparticle and intraparticle interaction, which can be regulated by the shell thickness and core size. It is also influenced significantly by shell materials. The shell materials are further affected by the iron-group metal, core size, material type, and crystalline structures. Furthermore, the shell structure, like the shell thickness and crystallinity, has a substantial influence on the core–shell composites.

The magnetization loops of the nanocomposite/ core-shell samples are the inclusive loop of the hard and soft magnetic materials [20, 22, 34, 35]. The magnetic moments of both phases rotate with each other. This can be attributed to their external magnetic field and consequently, the demagnetization and magnetization of the investigated nanoparticles [36] The main issues to regulate the magnetization of the core-shell samples are the exchange coupling interaction and dipolar interaction. Han et al.[37] has been studied the exchange coupling interaction that created at the interface between soft-hard, hard-hard, and soft-soft grains.

The value of saturation magnetization (M_s), remanent magnetization, (M_r) and coercivity (H_c) for the $La_2Fe_2O_6/CoFe_2O_4$ nanocomposites/ core–shell is lower compared with that of $CoFe_2O_4$ samples as detected in Table 1. This is due to the existence of the $La_2Fe_2O_6$ layer, which exhibits diluted magnetic properties as well as the presence of the canted spins [38, 39]. The interparticle exchange between the core and canted surface spins is the main reason for the small magnetization of the samples.

The porosity [40], as well as the thin shell thickness, have a great effect on the magnetization of the core/shell nanoparticles as illustrated in Fig. 6 [41]. The minimum and uniform shell thickness is obtained for S3 which has improved magnetization compared to S2.

Dramatic variation in the Coercivity is detected in Table 1. The sample S3 has H_c of 1560 Oe rather than the 378, and 459 Oe for the S1 and S2 samples respectively. The strong exchange coupling in addition to the alignment of the magnetic moments in parallel with each other enhances the magnetization of the system [34].

Finally, as shown from the Table the S3 has maximum magnetic parameters compared to S1 and S2 samples. This is due to the presence of cobalt as a shell not as a core.

Table 1

Saturation magnetization (M_s), Remanent magnetization (M_r), Coercivity (H_c), Energy loss, squareness (M_r/M_s), Anisotropy constant (K), and Magnetic moment (n_B)

Sample	M_s (emu/g)	M_r (emu/g)	H_c (Oe)	energy loss (erg/g) x 10^3	M_r/M_s	K	n_B
La ₂ Fe ₂ O ₆	1.062	0.182	305	2018	0.171	337.41	0.09
CoFe ₂ O ₄	66.847	31.114	1641	337	0.465	114290	2.81
S1	13.501	2.0785	378	19.175	0.154	5321	0.96
S2	11.105	1.5760	459	18.520	0.142	5311	0.79
S3	20.365	9.4571	1560	95.836	0.463	33104	1.46

Moreover, the studied samples have a squareness ratio (M_r/M_s) < 0.5 matching to multi-domain structure [42]. Furthermore, the obtained value of the (M_r/M_s) for CoFe₂O₄ and S3 is close to 0.5 indicating the uniaxial anisotropy contribution created by internal strains[43].

On the other side, the preparation conditions have the advantage of decreasing the values of the switching field distribution (SFD) for the core- shell nanoparticles. The SFD is another significant magnetic parameter that can be defined from the following equation [44]

$$SFD = \Delta H / H_c \quad (1)$$

Where ΔH is the full width at $\frac{1}{2}$ maximum of the dM/dH plot. The first- order reversal curves of the magnetization are utilized to testified the cooperation between the core and shell nanocomposites. As shown in Fig. 7: b a high broad single peak around H_c is observed corresponding to the exchange-coupled composite. In general, the noise in recordings and optimal bias current are the main issues accompanying the SFD. One of the origins of SFD is particle shape distribution. This is due to the fact that the shape anisotropy is partially responsible for the coercivity [45, 46].

The preparation methods of the studied samples are the other reasonable parameter for the detected difference in the SFD. This is because interparticle interaction between the stacked particles causes the cooperative magnetization switching between them [47].

The value of SFD is found to be 7.65, 7.16, 7.6, and 2.65 for La₂Fe₂O₆, S1, S2, and S3 respectively. Upon the previous arguments, the small SFD value for the S3 core-shell can be attributed to an intrinsic magnetic nature like shell homogeneity or crystallinity. which needs additional study. This investigation provides an overview of the use of the core-shell S3 for high-density recording.

The adsorption isotherm is a significant tool to adjust the use of core-shell as adsorbents. The data of Cr (III) adsorption on the synthesized S1, S2, and S3 nanoparticles is applied to the Freundlich [48, 49]

Langmuir[50, 51], and Temkin[52] isotherm models as detected from the following equations and illustrated in Fig. 8:a-c.

$$\text{Langmuir:} \quad \frac{C_e}{q_e} = \frac{1}{K_L q_m} + \frac{1}{q_m} C_e \quad (2)$$

$$\text{Freundlich:} \quad \text{Log } q_e = \text{Log } K_F + \frac{1}{n} \text{Log } C_e \quad (3)$$

$$\text{Temkin:} \quad q_e = a + b \ln C_e \quad (4)$$

Where C_e , equilibrium metal concentration; q_e and q_m are the amount of metal ion adsorbed per specific amount of adsorbent (mg/g) and the maximum adsorption capacity (mg/g) respectively. K_L and K_F are constants associated with the adsorptive capacity and the affinity between adsorbate and adsorbent. The equilibrium binding constant is "a" (g^{-1}) while, b is correlated to the heat of adsorption (J/ mol).

Among the studied models, the Freundlich model fitted well with correlation coefficients of 0.97, 0.98, 0.96, and 0.96 for $\text{La}_2\text{Fe}_2\text{O}_6$, S1, S2, and S3 samples respectively. The Freundlich isotherm model is a more convenient one for the adsorption in the core-shell system, indicating that the sorption of Cr (III) is multilayer physisorption in the heterogeneous surface. While $\text{La}_2\text{Fe}_2\text{O}_6$ is a combination of homogenous monolayer and multilayer.

The obtained value of n is found to be in the range of $1 < n < 10$ indicates a favorable sorption process as well as the heterogeneity surface of the investigated samples [53]. Different parameters determined from the investigated models are given in the inset of Fig. 8.

The elimination efficiency of Cr III ions in an aqueous solution is clearly influenced by pH, as shown in Fig. 9: a. The maximum Cr III removal is attained by increasing pH from 4 to 8 at room temperature.

However, at low pH values, Cr (III) ions are mostly adsorbed by the prepared samples. When the pH value is > 8.0 , OH^- ions are increased, and $\text{Cr}(\text{OH})_3$ is created. Cr (III) is removed by the investigated nanoparticles as well as the $\text{Cr}(\text{OH})_3$ precipitates. The maximum removal % of Cr (III) at pH 7 for $\text{La}_2\text{Fe}_2\text{O}_6$, S1, S2 and S3 is nearly 90. %, 98.49%, 95%, and 99.3 % respectively. The high removal % of the core-shell S3 samples can be elucidated based on XPS results. The crucial information about the $\text{O}^{2-}-\text{Fe}^{3+}-\text{O}^{2-}$ and $\text{O}^{2-}-\text{Co}^{2+}-\text{O}^{2-}$ that have different electron densities and more oxygen vacancies are obtained from XPS data as mentioned before.

On the other side, contact time is a crucial parameter for the water treatment system. In the examined case, the increase of adsorption with increasing the contact time as illustrated in Fig. 9:b, and the maximum adsorption is detected at 60 min.

Additionally, the rate of chromium ion elimination can be clarified based on the variation of adsorption sites with time.

The first -order, the pseudo-second-order (PSO), and the intraparticle diffusion equations are the three models utilized for interpreting the investigational results [54, 55] .

The PSO model [56] can be written as:

$$\frac{t}{qt} = \frac{1}{k_2 q_2^2} + \frac{1}{q_2} t \quad (6)$$

The maximum adsorption capacity (mol g^{-1}) for the PSO adsorption is q_2 ; The rate constant of the PSO model for the adsorption development ($\text{g mol}^{-1} \text{min}^{-1}$) is K_2

In this model, the removal from a solution can be attributed to the physico-chemical interactions between the two phases[57].

The kinetic parameters are calculated and illustrated in Table 2. For the second-order kinetics, the correlation coefficients (R^2) > 0.98. The PSO kinetic model fits the investigational results. Consequently, Cr (III) ion adsorption on magnetic ferrites is a multistep progression involving both sorption on the adsorbent's exterior surface and diffusion into its [58].

Table 2
The PSO kinetic model parameters.

models	parameter	La ₂ Fe ₂ O ₆	S1	S2	S3
pseudo-second-order kinetic model	q ₂ (mg/g)	14.104	12.610	11.99	12.9199
	K ₂ (mg/g.min)	0.0018	0.0042	0.0041	0.0039
	R ²	0.990	0.9800	0.9900	0.9830

Conclusion

The attempt to synthesize a core-shell of La₂Fe₂O₆ / CoFe₂O₄ nanoparticles is succeeded for the third method. While the incomplete core-shell is obtained for the second method.

The core-shell structure is confirmed from HRTEM images.

A significant difference in the prepared samples is detected due to their numerous preparation techniques.

The investigated core–shell nanoparticles exhibit higher magnetic anisotropies compared to the pure La₂Fe₂O₆.

The suitability of novel adsorbent, core-shell nanocomposites for heavy metal removal such as Cr III from the wastewater is achieved. S3 sample is suggested as a promising candidate for data storage devices and waste water treatment.

The obtained results are fitted to several models, and the Freundlich model is the best one for Cr III with R^2 values 0.97, 0.98, 0.96, and 0.96 for $\text{La}_2\text{Fe}_2\text{O}_6$, S1, S2, and S3.

Declarations

Conflict of interest: The authors declare that they have no conflict of interest.

ASRT Acknowledgments

This paper is supported financially by the Academy of Scientific Research and Technology (ASRT), Egypt, under initiatives of Science Up Faculty of Science (Grant No. 6621).

References

1. A. M. El-Toni, M. A. Habila, J. P. Labis, Z. A. AlOthman, M. Alhoshan, A. A. Elzatahry, and F. Zhang, *Nanoscale* **8**, 2510 (2016).
2. N. S. and Y. Zhang, *Recent Patents Biomed. Eng.* **1**, 34 (2008).
3. G. Kandasamy, *Nanotechnology* **30**, 502001 (2019).
4. K. C. Verma, M. Singh, R. K. Kotnala, and N. Goyal, *J. Magn. Mater.* **469**, 483 (2019).
5. H. Wang, L. Chen, Y. Feng, and H. Chen, *Acc. Chem. Res.* **46**, 1636 (2013).
6. H. Amouri, C. Desmarets, and J. Moussa, *Chem. Rev.* **112**, 2015 (2012).
7. L. J. Lauhon, M. S. Gudixsen, D. Wang, and C. M. Lieber, *Nature* **420**, 57 (2002).
8. H. H. Park, K. Woo, and J.-P. Ahn, *Sci. Rep.* **3**, 1497 (2013).
9. M. A. Peña and J. L. G. Fierro, *Chem. Rev.* **101**, 1981 (2001).
10. I. H. Lone, J. Aslam, N. R. E. Radwan, A. H. Bashal, A. F. A. Ajlouni, and A. Akhter, *Nanoscale Res. Lett.* **14**, 142 (2019).
11. D. Serrate, J. ~M. DeTeresa, and M. ~R. Ibarra, *J. Phys. Condens. Matter* **19**, 23201 (2007).
12. H. Kato, T. Okuda, Y. Okimoto, Y. Tomioka, K. Oikawa, T. Kamiyama, and Y. Tokura, *Phys. Rev. B* **69**, 184412 (2004).

13. T. Kimura, H. Sawada, and K. Terakura, **395**, 677 (1998).
14. M. Madhukara Naik, H. S. Bhojya Naik, G. Nagaraju, M. Vinuth, K. Vinu, and R. Viswanath, Nano-Structures and Nano-Objects **19**, 100322 (2019).
15. S. M. Ansari, S. R. Suryawanshi, M. A. More, D. Sen, Y. D. Kolekar, and C. V Ramana, Chem. Phys. Lett. **701**, 151 (2018).
16. B. J. Rani, M. Ravina, B. Saravanakumar, G. Ravi, V. Ganesh, S. Ravichandran, and R. Yuvakkumar, Nano-Structures & Nano-Objects **14**, 84 (2018).
17. J. Cheon, J.-I. Park, J. Choi, Y. Jun, S. Kim, M. G. Kim, Y.-M. Kim, and Y. J. Kim, Proc. Natl. Acad. Sci. U. S. A. **103**, 3023 LP (2006).
18. G. C. Lavorato, E. Lima, H. E. Troiani, R. D. Zysler, and E. L. Winkler, Nanoscale **9**, 10240 (2017).
19. S. M. Yusuf, P. K. Manna, M. M. Shirolkar, S. K. Kulkarni, R. Tewari, and G. K. Dey, J. Appl. Phys. **113**, 173906 (2013).
20. H. Zeng, S. Sun, J. Li, Z. L. Wang, and J. P. Liu, Appl. Phys. Lett. **85**, 792 (2004).
21. J.-H. Lee, J. Jang, J. Choi, S. H. Moon, S. Noh, J. Kim, J.-G. Kim, I.-S. Kim, K. I. Park, and J. Cheon, Nat. Nanotechnol. **6**, 418 (2011).
22. O. Masala, D. Hoffman, N. Sundaram, K. Page, T. Proffen, G. Lawes, and R. Seshadri, Solid State Sci. **8**, 1015 (2006).
23. E. E. Ateia, A. T. Mohamed, and H. Elshimy, Appl. Nanosci. **10**, 1489 (2020).
24. E. E. Ateia, A. A. El-Bassuony, G. Abdelatif, and F. S. Soliman, J. Mater. Sci. Mater. Electron. **28**, (2017).
25. B. Xu, G. Zhou, and X. Wang, NPG Asia Mater. **7**, e164 (2015).
26. E. Vedmedenko, *Competing Interactions and Patterns in Nanoworld The Chemistry of Nanomaterials Nanoparticles Introduction to Nanotechnology* (2007).
27. W. P. Wang, H. Yang, T. Xian, and J. L. Jiang, Mater. Trans. **53**, 1586 (2012).
28. D. K. Pradhan, S. Kumari, V. S. Puli, P. T. Das, D. K. Pradhan, A. Kumar, J. F. Scott, and R. S. Katiyar, Phys. Chem. Chem. Phys. **19**, 210 (2017).
29. J. Li, M. Xu, G. Yao, and B. Lai, Chem. Eng. J. **348**, 1012 (2018).
30. B. Aguilar, T. E. Soto, J. de la T. Medina, and O. Navarro, Phys. B Condens. Matter **556**, 108 (2019).
31. Z. Zhou, Y. Zhang, Z. Wang, W. Wei, W. Tang, J. Shi, and R. Xiong, Appl. Surf. Sci. **254**, 6972 (2008).

32. M. Béjaoui, A. Elmhamdi, L. Pascual, P. Pérez-Bailac, K. Nahdi, and A. Martínez-Arias, *Catalysts* **11**, 15 (2020).
33. K. ZHAO, Y. SHEN, F. HE, Z. HUANG, G. WEI, A. ZHENG, H. LI, and Z. ZHAO, *J. Rare Earths* **34**, 1032 (2016).
34. F. Song, X. Shen, M. Liu, and J. Xiang, *J. Solid State Chem.* **185**, 31 (2012).
35. P. Maltoni, T. Sarkar, G. Barucca, G. Varvaro, F. Locardi, D. Peddis, and R. Mathieu, *J. Phys. Chem. C* **125**, 5927 (2021).
36. J. M. Soares, V. B. Galdino, and F. L. A. Machado, *J. Magn. Magn. Mater.* **350**, 69 (2014).
37. G. B. Han, R. W. Gao, S. Fu, W. C. Feng, H. Q. Liu, W. Chen, W. Li, and Y. Q. Guo, *Appl. Phys. A* **81**, 579 (2005).
38. T. Ozkaya, M. S. Toprak, A. Baykal, H. Kavas, Y. Köseoğlu, and B. Aktaş, *J. Alloys Compd.* **472**, 18 (2009).
39. Z. L. Liu, Y. J. Liu, K. L. Yao, Z. H. Ding, J. Tao, and X. Wang, *J. Mater. Synth. Process.* **10**, 83 (2002).
40. N. O. Núñez, P. Tartaj, M. P. Morales, P. Bonville, and C. J. Serna, *Chem. Mater.* **16**, 3119 (2004).
41. E. E. Carpenter, C. Sangregorio, and C. J. O'Connor, *IEEE Trans. Magn.* **35**, 3496 (1999).
42. M. S. A. Darwish, H. Kim, H. Lee, C. Ryu, J. Young Lee, and J. Yoon, *Nanomater.* (Basel, Switzerland) **10**, 991 (2020).
43. T. Ibusuki, S. Kojima, O. Kitakami, and Y. Shimada, *IEEE Trans. Magn.* **37**, 2223 (2001).
44. E. E. Ateia, A. T. Mohamed, M. Maged, and A. Abdelazim, *Appl. Phys. A* **126**, 669 (2020).
45. G. Long, H. Zhang, D. Li, R. Sabirianov, Z. Zhang, and H. Zeng, *Appl. Phys. Lett.* **99**, 202103 (2011).
46. H. Kirchmayr, in *Second Edi (Encyclopedia of Materials: Science and Technology*, Oxford, 2001), pp. 4754–4757.
47. S. Singamaneni, V. N. Bliznyuk, C. Binek, and E. Y. Tsympal, *J. Mater. Chem.* **21**, 16819 (2011).
48. N. Ayawei, A. N. Ebelegi, and D. Wankasi, *J. Chem.* **2017**, 3039817 (2017).
49. H. K. Boparai, M. Joseph, and D. M. O'Carroll, *J. Hazard. Mater.* **186**, 458 (2011).
50. S. K. Maji, S.-W. Wang, and C.-W. Liu, *Desalin. Water Treat.* **51**, 7775 (2013).
51. F. Haghseresht and G. Q. Lu, *Energy & Fuels* **12**, 1100 (1998).

52. M. T. Bankole, A. S. Abdulkareem, I. A. Mohammed, S. S. Ochigbo, J. O. Tijani, O. K. Abubakre, and W. D. Roos, *Sci. Rep.* **9**, 4475 (2019).
53. F. Togue Kamga, *Appl. Water Sci.* **9**, 1 (2018).
54. N. Kannan and M. M. Sundaram, *Dye. Pigment.* **51**, 25 (2001).
55. R. Qadeer, *Adsorption* **11**, 51 (2005).
56. Y. S. Ho and G. Mckay, *Process Saf. Environ. Prot.* **76**, 183 (1998).
57. H. Wang, A. Zhou, F. Peng, H. Yu, and J. Yang, *J. Colloid Interface Sci.* **316**, 277 (2007).
58. V. K. Gupta, D. Pathania, S. Sharma, S. Agarwal, and P. Singh, *J. Mol. Liq.* **177**, 343 (2013).

Figures

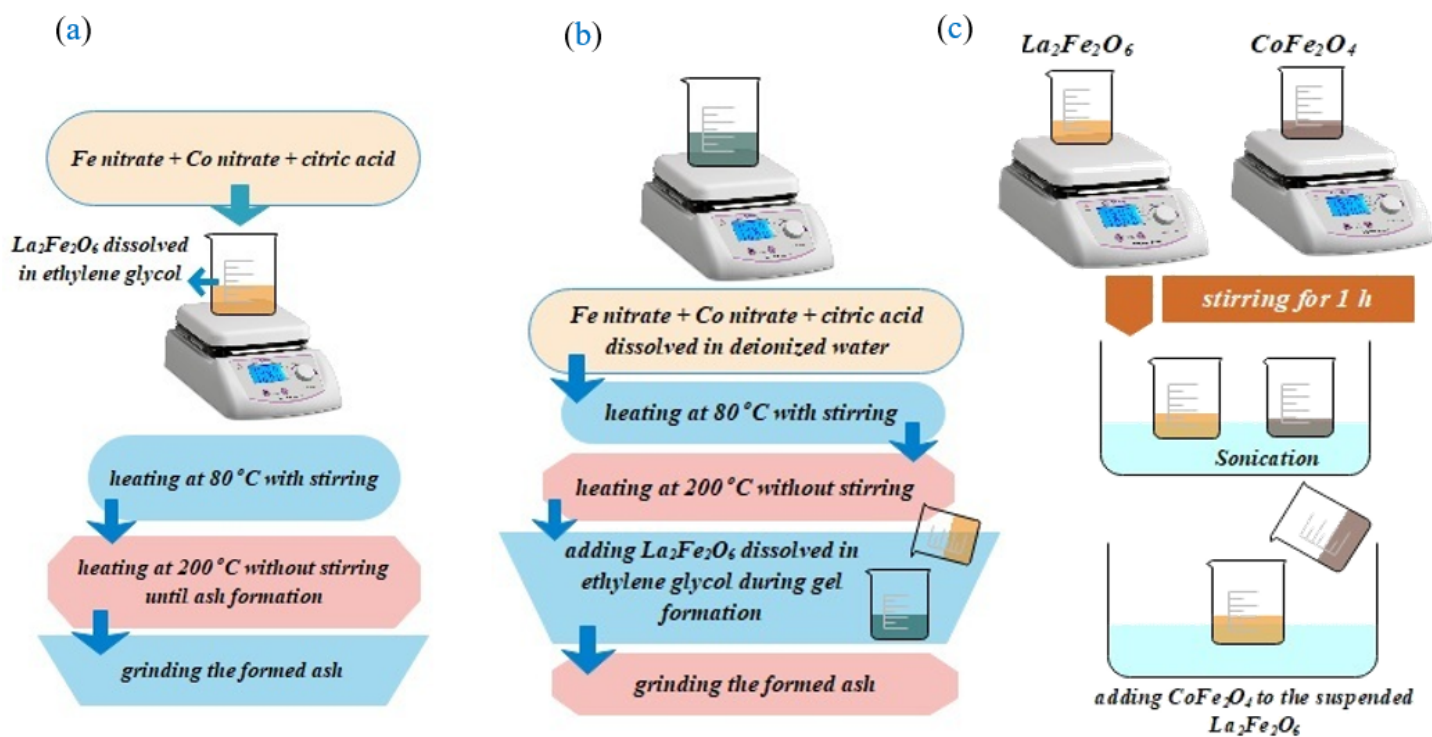


Figure 1

Schematic presentation of the preparation method for (a)S1, (b) S2 and (c) S3.

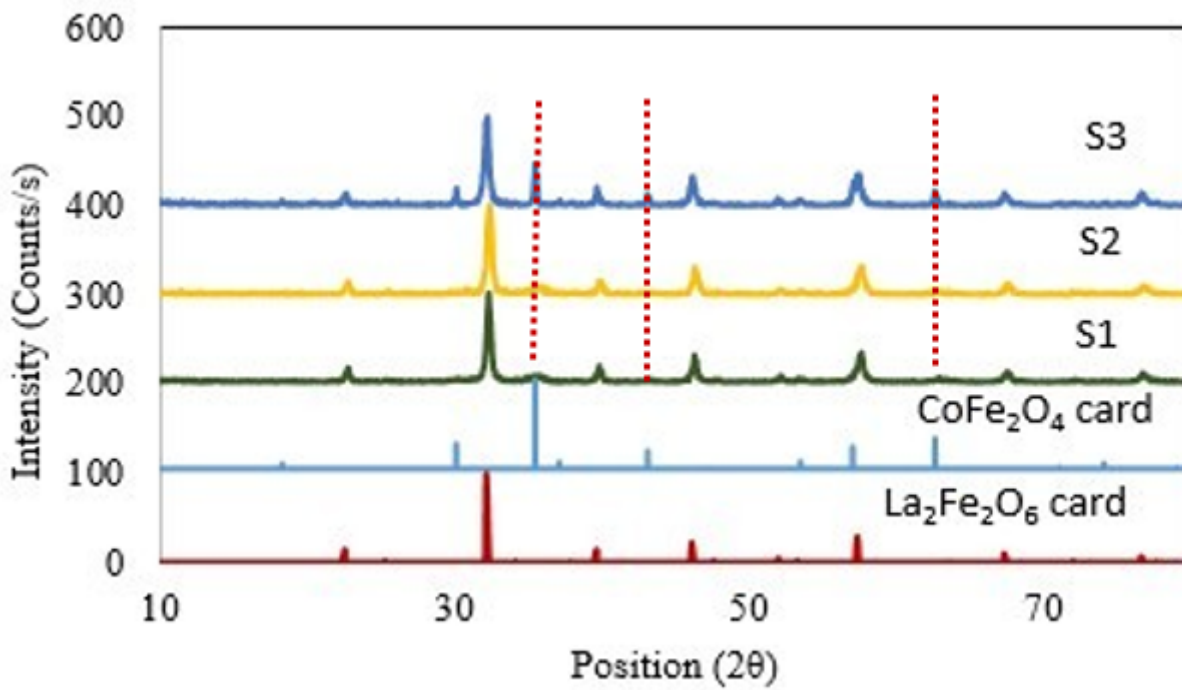


Figure 2

the XRD pattern of the prepared nanocomposites samples

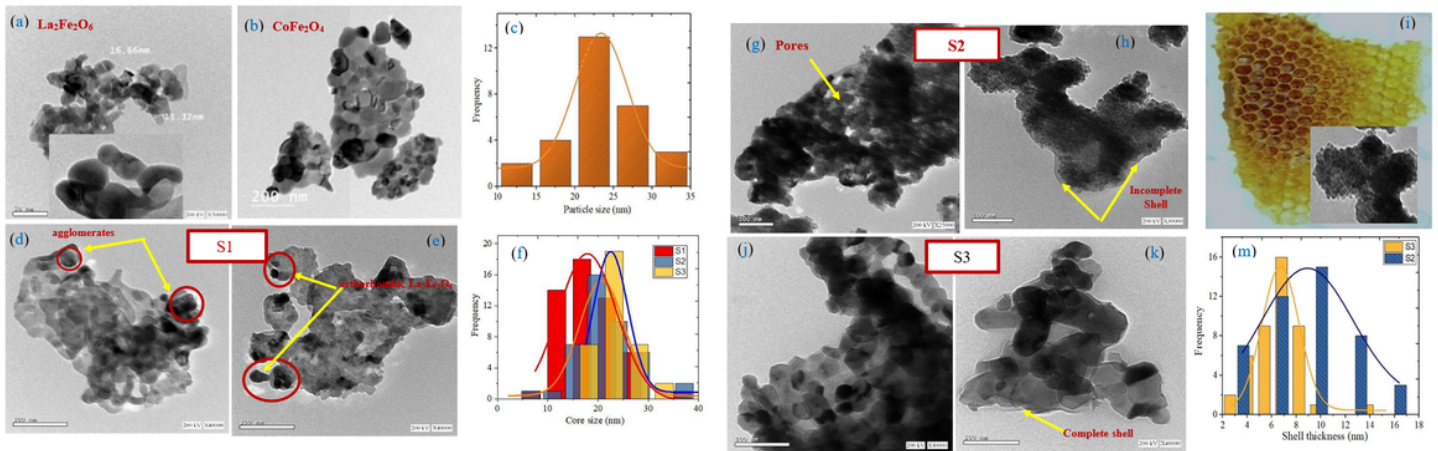


Figure 3

HRTEM images for (a) $\text{La}_2\text{Fe}_2\text{O}_6$, (b) CoFe_2O_4 , (d, e) S1, (g, h) S2, and (j, k) S3 samples and the histogram for (c) particle size distribution of $\text{La}_2\text{Fe}_2\text{O}_6$, (f) core size distribution, (m) shell thickness distribution. (i) Honey comb shape with matching morphology for S2.

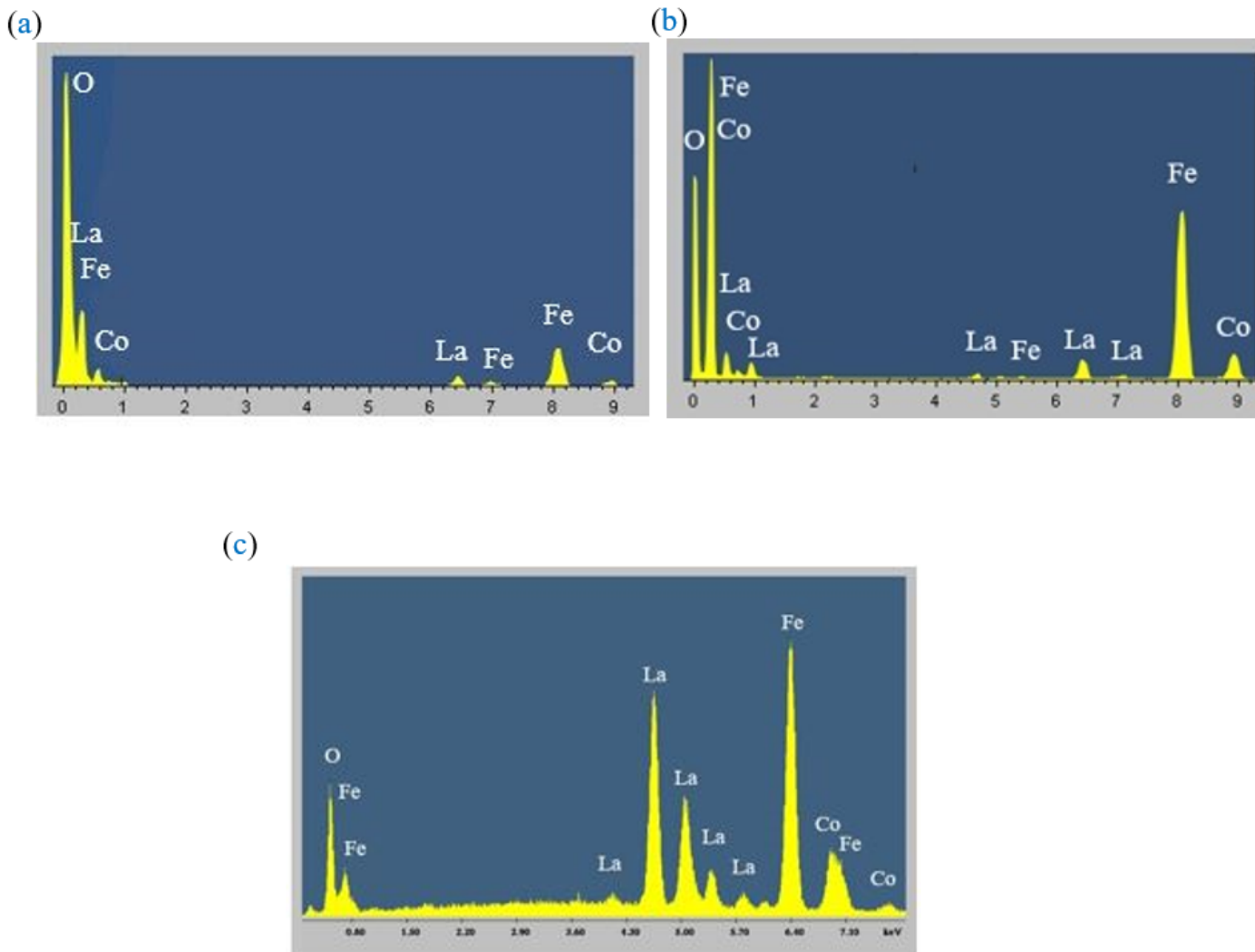


Figure 4

EDAX spectrum for (a) S1 , (b)S2, and (c)S3 nanoparticles

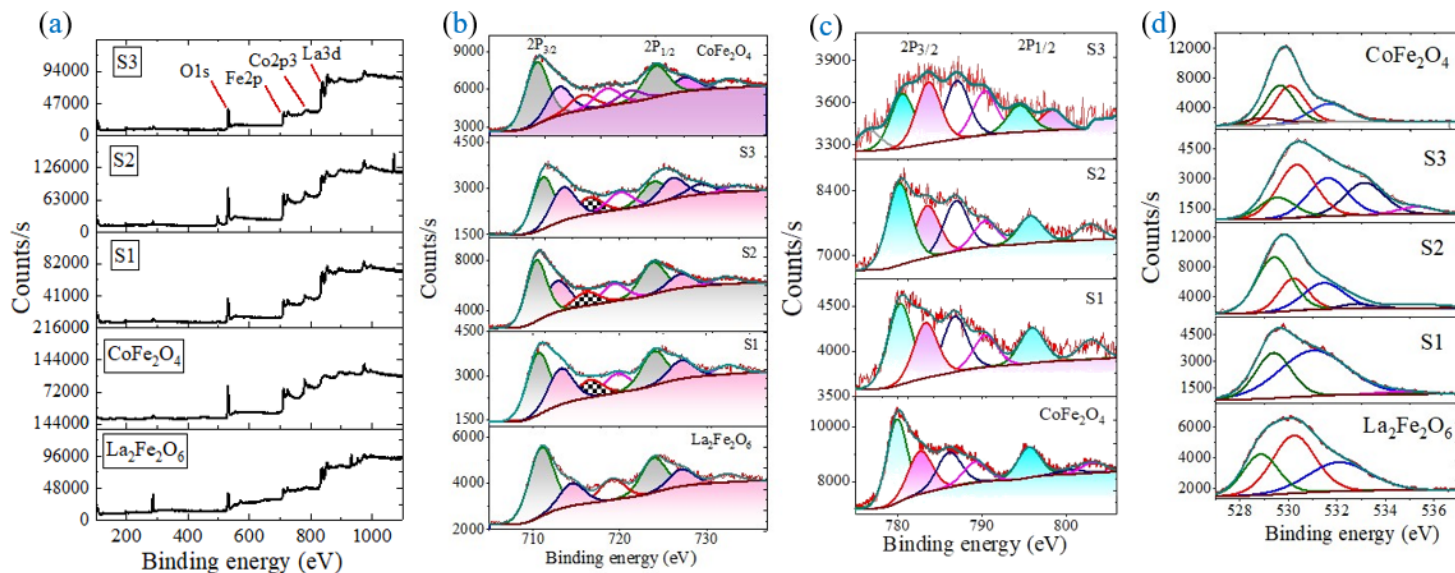


Figure 5

a-d) The XPS spectra of the investigated samples for (a) survey, (b) Fe2p, (c)Co2p3 and (d) O1s

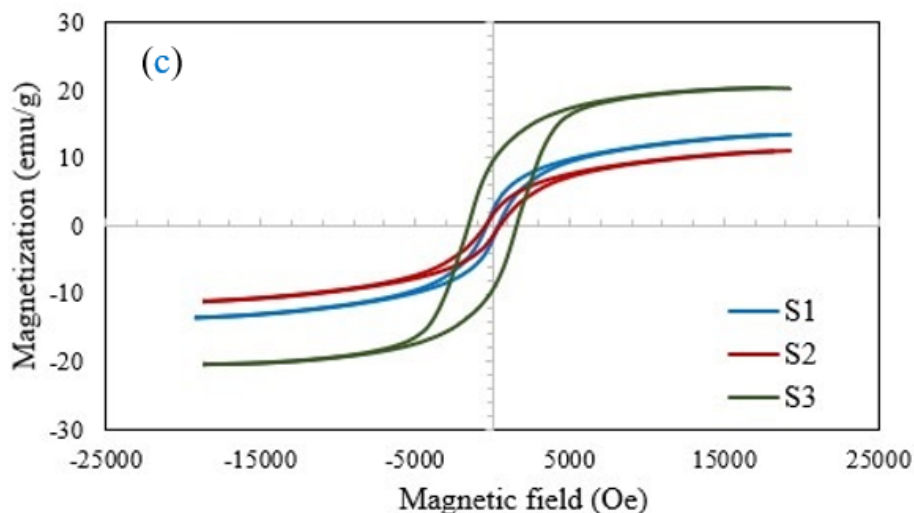
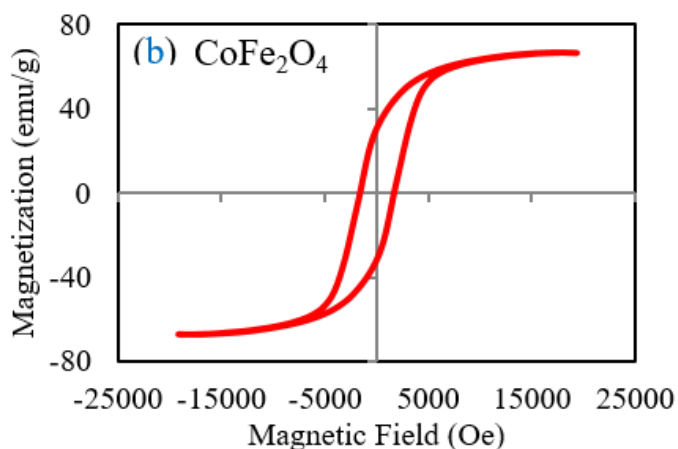
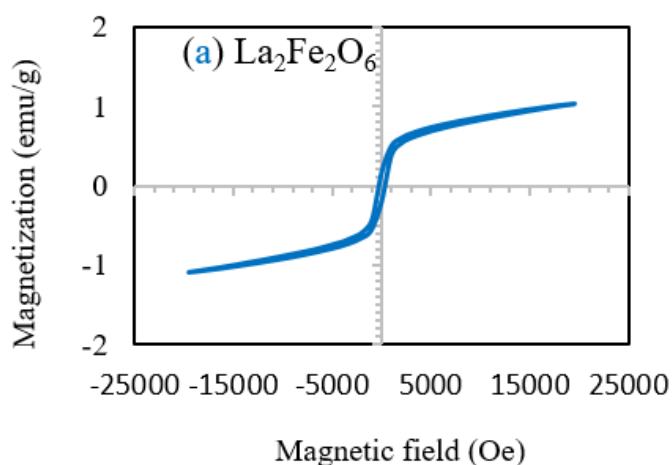


Figure 6

VSM profile for the studied samples

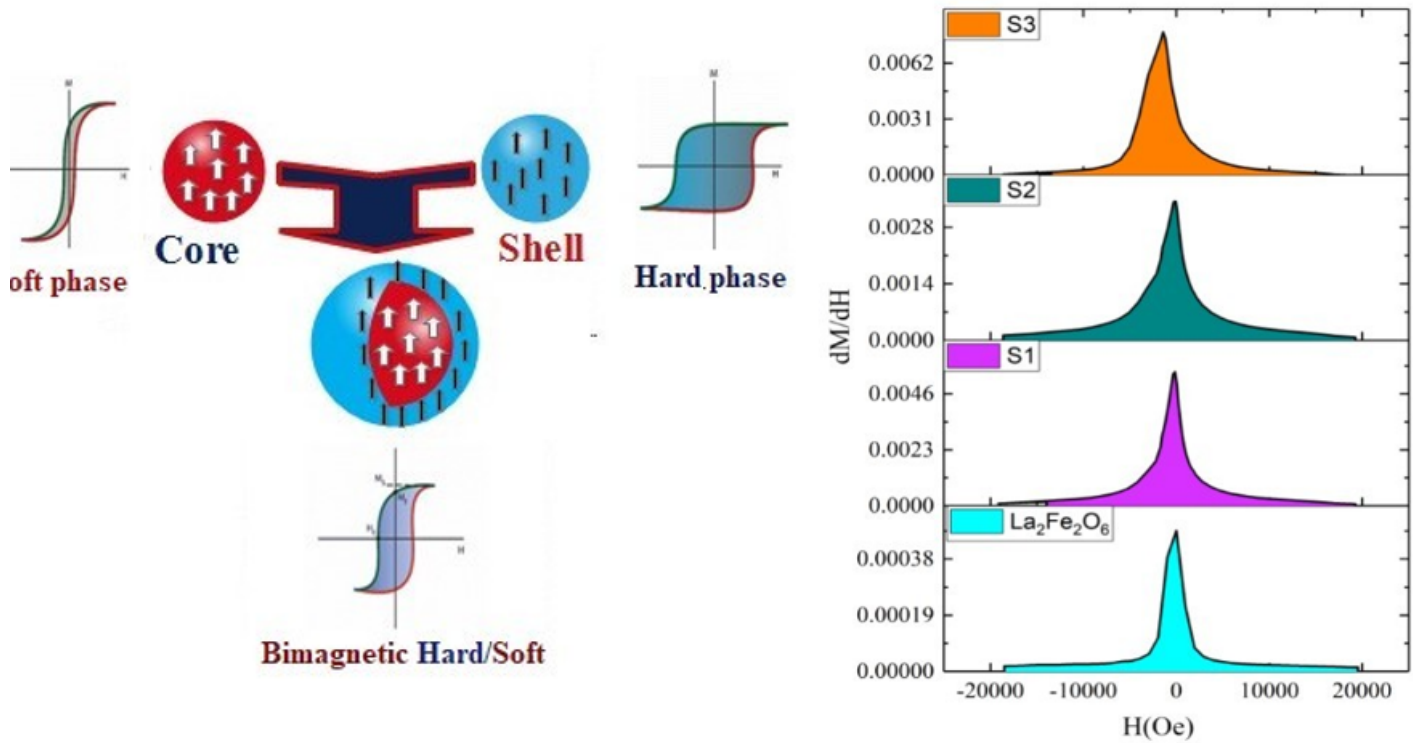


Figure 7

a-b (a) schematic illustration for the exchange coupling in magnetic hard/soft core shell and (b) first-order deferential curves of the magnetization

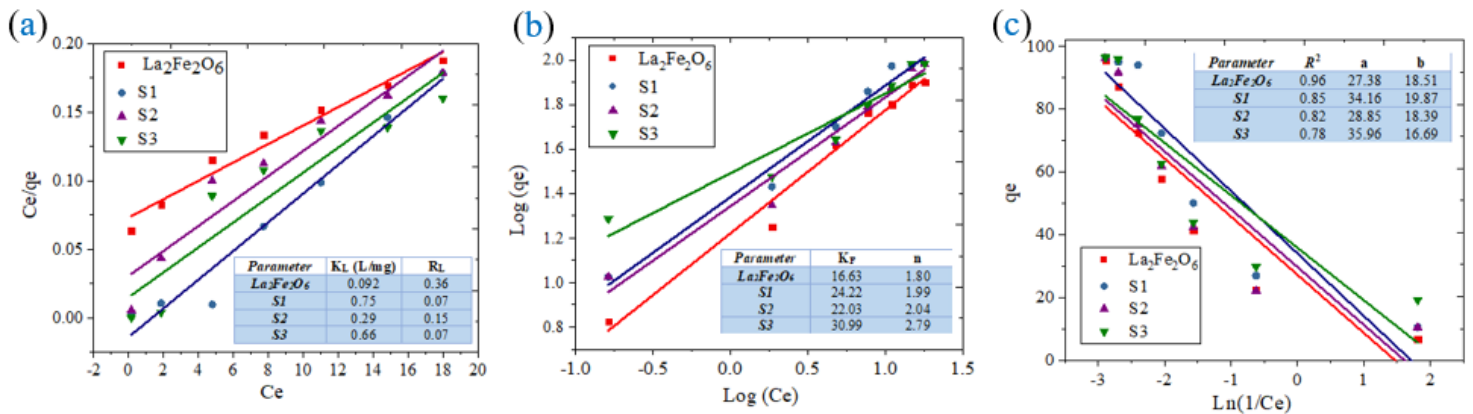


Figure 8

Represent the fitting of the obtained data with (a) The Langmuir isotherm, (b) The Freundlich isotherm, and (c) The Temkin isotherm. The inset table contain the obtained isotherm parameters.

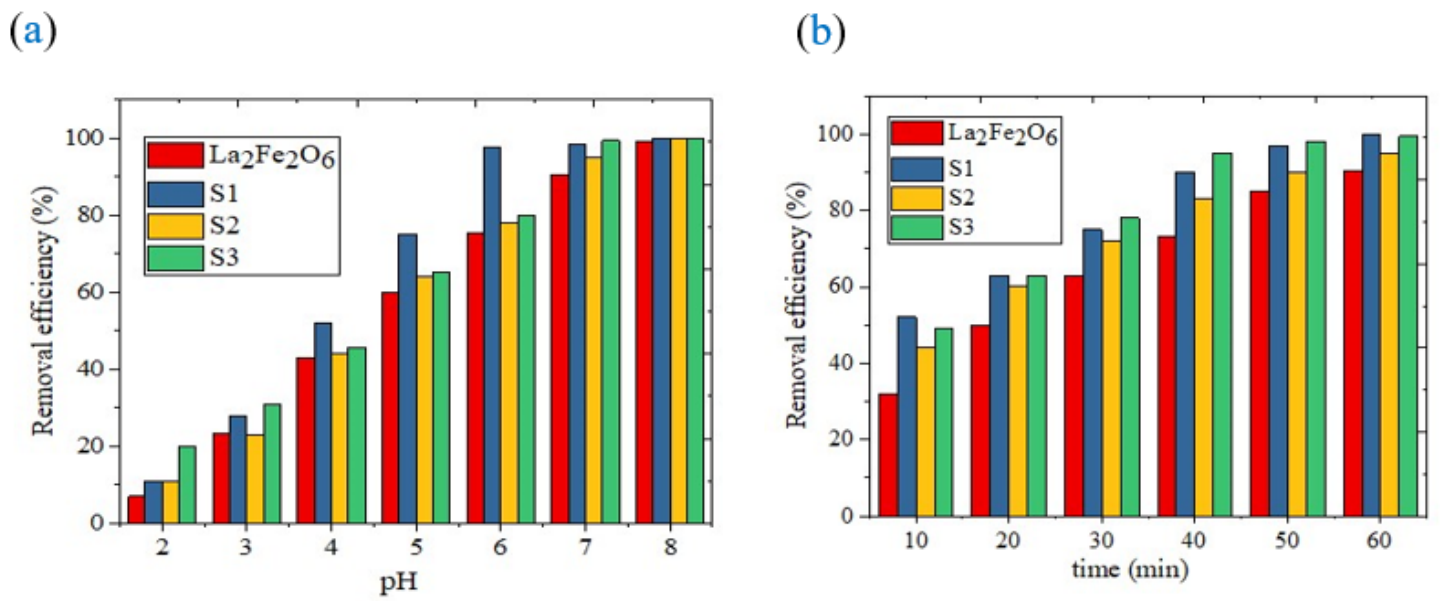


Figure 9

The dependence of the removal efficiency on (a) pH (b) The contact time.

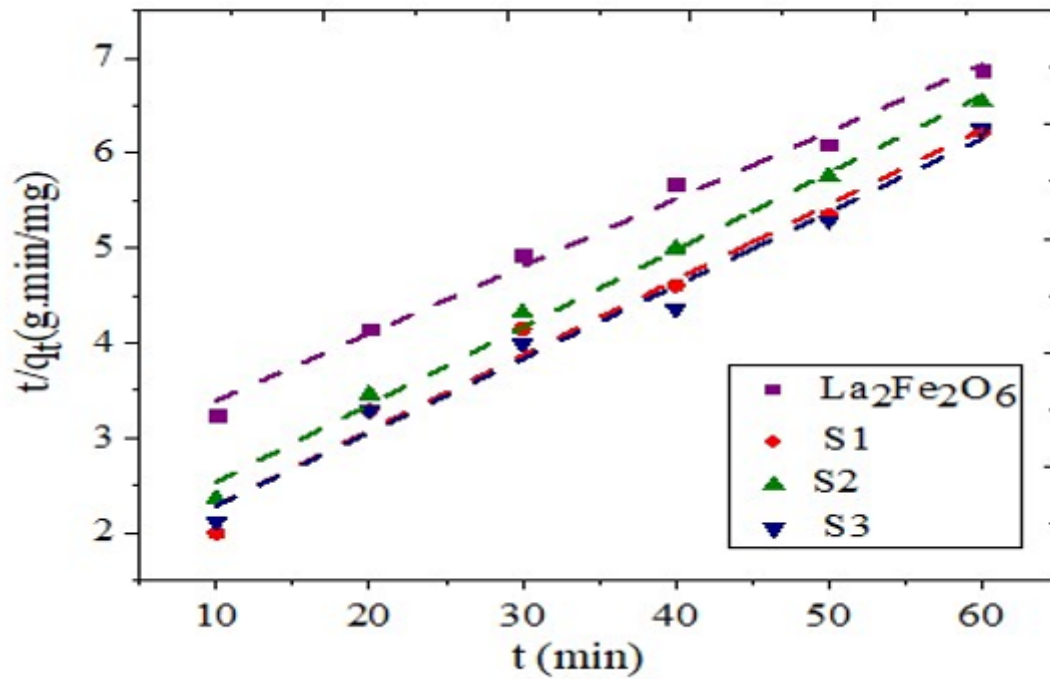


Figure 10

The fitting of the investigational data with the PSO.